



## CsPbI<sub>3</sub> perovskite solar cell and decoding its skink feature in J-V curve



R Thandaiah Prabu <sup>a</sup>, Satyajeet Sahoo <sup>b</sup>, K. Valarmathi <sup>g</sup>, A Gnana Sagaya Raj <sup>f</sup>, Pranay Ranjan <sup>c</sup>, Atul Kumar <sup>d,\*</sup>, Amel Laref <sup>e</sup>

<sup>a</sup> Department of Electronics and Communication Engineering, Saveetha School of Engineering, SIMATS, Chennai, 602105, India

<sup>b</sup> Department of Electronics and Communication Engineering, Vignan's Foundation for Science, Technology and Research Vadlamudi, Guntur, Andhra Pradesh, 522213, India

<sup>c</sup> Department of Metallurgical and Materials Engineering, IIT, Jodhpur, Rajasthan, 342037, India

<sup>d</sup> Department of Electronics and Communication Engineering, Koneru Lakshmaiah Education Foundation, Greenfields, Vaddeswaram, Guntur, Andhra Pradesh, 522502, India

<sup>e</sup> Physics Department, Faculty of Science, King Saudi University, Riyadh, 11451, Saudi Arabia

<sup>f</sup> Department of Mechanical Engineering, Mohan Babu University, Tirupati, Andhra Pradesh, 517102, India

<sup>g</sup> School of Computer Science and Engineering, Vellore Institute of Technology, Chennai, 600127, India

### ARTICLE INFO

#### Keywords:

Perovskite

Skink

Band offset

Rollover

Defects signatures

### ABSTRACT

Skink feature in the current density-voltage (J-V) characteristic is observed in an inorganic perovskite CsPbI<sub>3</sub> thin film solar cell. The fabricated CsPbI<sub>3</sub> solar cell attained maximum efficiency of 8.8% under one sun illumination. It showed a prominent skink phenomenon in the positive biasing region near the open-circuit voltage in the illuminated J-V curve. Skink is a curvilinear s-shape feature in J-V that dramatically deteriorate the fill factor. This study explored the probable cause of such a skink feature by theoretical modelling. It is observed that energy level mismatch, through a relatively high valence band offset (VBO) barrier at the hole transport layer HTL/perovskite junction along with a bulk defect in perovskite, replicates the skink feature in simulated J-V. We showed a one-to-one relation between the skink feature in the J-V curve and its steering parameters in the CsPbI<sub>3</sub> device. This one-to-one dependence provides a peek into the device's working and is of great help for understanding the defect physics of experimental devices.

### 1. Introduction

Hybrid organic-inorganic perovskite solar cell has shown tremendous growth in efficiency since their inception [1] and has surpassed the long-standing technologies of Cu(In<sub>1-x</sub>Ga<sub>x</sub>)Se<sub>2</sub> and CdTe, and is now nearly equalizing silicon solar cells (26.7%) [2] in term of lab scale performance. However, perovskite is yet to make its commercial debut owing to unresolved challenges of stability, lifetime, current density-voltage J-V hysteresis, and other performance-related issues. [3–5] Stability issues are severe limiting issues, mainly due to hygroscopicity, volatility, thermal and chemical instability of organic cations. [6] It is likely resolved by replacing the organic part with inorganic-based perovskite. [7] However, these inorganic replacements can boost stability but lack performance due to complex material-based bulk and interfacial recombination. [8] An inorganic perovskite solar cell of caesium lead triiodide (CsPbI<sub>3</sub>) is explored for its photovoltaic action. [9–12] Perovskite solar cells have a general HTL(hole transport

layer)/Perovskite/ETL(electron transport layer) configuration. The perovskite is the photoactive absorber layer with a known thickness of ~600 nm. HTL (hole transport layer) is a *p*-type layer, selectively collecting and transporting photogenerated holes to the anode metal contact. ETL (electron transport layer) is an *n*-type layer that selectively collects photogenerated electrons and transports them to cathode metal contact. Ideally, the HTL and ETL have high respective carrier density and high bandgap. In an ideal solar cell, perovskite has a suitable bandgap in the visible region (bandgap of 1.5eV–1.7eV) [13], absorbing incident photons and generating electrons and holes with unity internal quantum efficiency. Owing to interfacial complexities in inorganic perovskite, despite possessing optimal bandgap, high optical absorption coefficient, panchromatic absorption of light, and long diffusion length, they show abnormalities in current density-voltage (J-V) plots. Skink and hysteresis are some of the persistent issues observed in perovskite J-V. [14] The complicated interface physics of hybrid organic-inorganic devices is possibly responsible for these observations. On the other hand,

\* Corresponding author.

E-mail addresses: [er.atul89@gmail.com](mailto:er.atul89@gmail.com), [atulkumar@kluniversity.in](mailto:atulkumar@kluniversity.in) (A. Kumar).

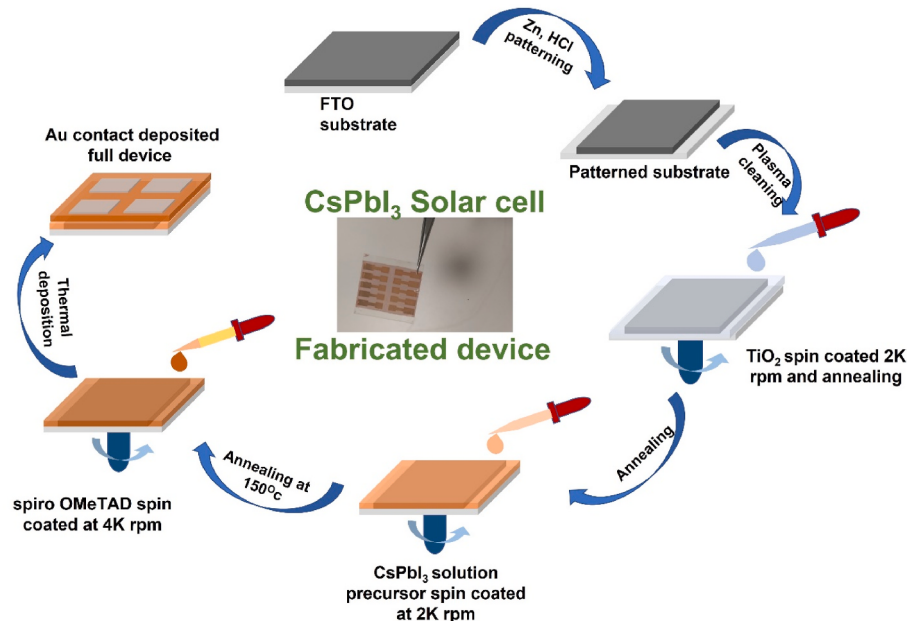


**Fig. 1.** The schematic of the fabrication steps involved and the optical image of the final device.

these abnormal features in J-V also reveal the underlying defect or dominant recombination mechanism. [15–17] It can be said that these J-V characterizations have signatures of imperfections present within the device. [18,19] These experimental device signals contain involved and implicit information about the device's internal recombination. [20] Earmarking the abnormal J-V feature to a specific recombination mechanism is complex. A one-to-one dependence of J-V features and their steering parameters uncovers faults in experimental devices and is of great help for understanding defect physics.

We fabricated an inorganic  $\text{CsPbI}_3$  perovskite solar cell device in the present study. Its electrical characterization shows J-V abnormality. The one-to-one relationship between the performance of an experimental perovskite device and theoretically assigning the probable recombination mechanism. We present a defect model to replicate abnormality and give the anomalous skink signature using the Poisson-Schrodinger-based device model of perovskite  $\text{CsPbI}_3$  solar cells. Section 2 describes the detailed experimental aspect of device fabrication and its characterization. The physical model with defects, which replicates experimentally observed skink features, is theoretically reproduced by assigning the parameters, and the recombination mechanism is thoroughly discussed in Section 3.

## 2. Methodology

Fabrication: We followed the literature procedure to prepare the  $\text{CsPbI}_3$  precursor solution. [21] The prepared solution of  $\text{Pb}(\text{AC})_2$ ,  $\text{CsI}$ , and  $\text{MAI}$  in DMF with a molar ratio of 1:2:1 are mixed. This precursor solution is used for spin-coating of  $\text{CsPbI}_3$  perovskite. Pre-patterned

fluorine doped tin oxide (FTO) substrate was sequentially ultrasonicated in acetone, deionized water, and isopropanol. A spin-coated thin  $\text{TiO}_2$  layer was deposited on the FTO substrate, followed by the annealing. The perovskite precursor solution was spin-coated at 2000 rpm on the  $\text{TiO}_2$ -coated FTO substrates, followed by rapid annealing at 150 °C for 5 min. After that, the HTL layer of spiro-OMeTAD solution (in 1 mL chlorobenzene, and adding 18  $\mu\text{L}$  of a stock solution of 520 mg/mL Li-TFSI in acetonitrile, 30  $\mu\text{L}$  4-tert-butyl pyridine) was spin-coated over the  $\text{CsPbI}_3$  at 4000 rpm for about 20 s. A metal contact (anode) of gold metal was deposited by thermal evaporation using the mask to form a complete device structure of FTO/ $\text{TiO}_2$ / $\text{CsPbI}_3$ /Spiro/Au. The fabrication steps are schematically shown in Fig. 1.

Characterization: Field emission scanning electron microscopy (FESEM) was done by Zeiss in backscattering mode to analyze the surface morphology, grain size, and cross-section structure of the device. The active area of the fabricated device was defined by a mask while depositing the gold contacts and is around  $1 \text{ cm}^2$ . X-ray diffraction, XRD (Rigaku) was performed to confirm the correct phase formation with Bragg Brentano geometry from 0 to 50° two theetha degrees. LabVIEW automated Keithley 2420 system measured J-V characteristics in a two-wire configuration with a voltage scan rate of 50, 25 mV/s. LabVIEW codes were written for controlling Keithly and Xenon lamps. Xenon lamp with AM 1.5G filter providing one sun illumination ( $100 \text{ mWcm}^{-2}$ ) is used for illumination. This illumination source is first calibrated with a Si photodiode. Theoretical studies are carried out by the one-dimensional simulation package of the solar cell capacitance simulator (SCAPS). [22–26] Detailed defect model and simulation parameters are comprehensively described. One can replicate our results using the same

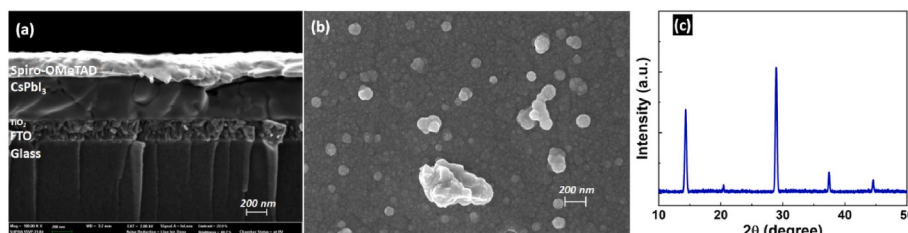


**Fig. 2(a).** The cross-sectional FESEM image showing different constituent layers and their thickness in the device. (b) The surface morphology of the spin-coated film. (c) The XRD diffraction pattern of the deposited  $\text{CsPbI}_3$  perovskite film.

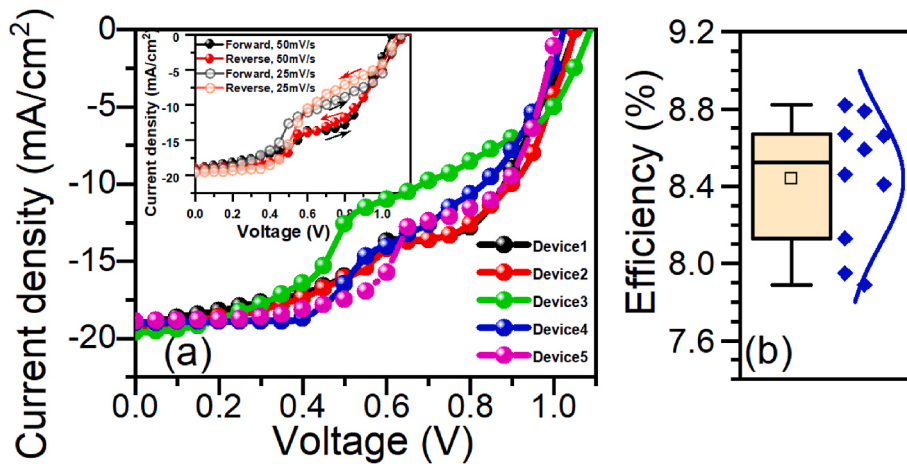


**Fig. 3(a).** The J-V characteristic of several devices with a prominent skink feature. The inset shows the forward and reversed scan at two different scan rates. (b) The scatter plot of the efficiency values of ten devices.

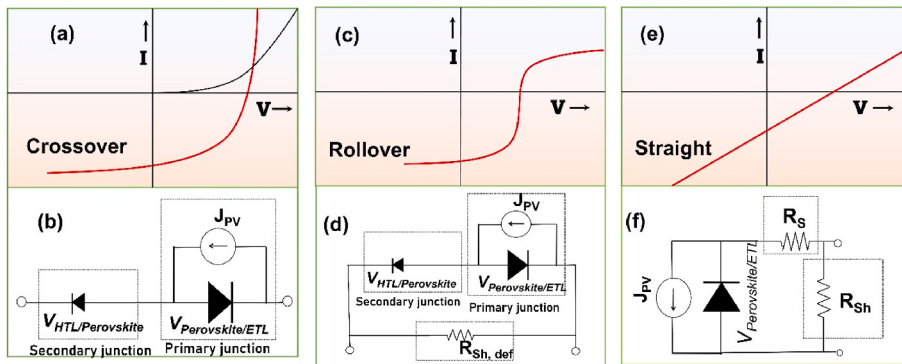


**Fig. 4(a).** The schematic of crossover (light and dark J-V crosses), (b) Diode model below shows the secondary diode which is responsible for crossover behaviour, (c) Rollover, current saturates after  $V_{OC}$ , (d) shows the secondary diode along with small  $R_{sh, def}$  (arising due to high bulk defect) which are responsible for rollover behaviour, and (e) Straight J-V curve where FF decreases due to suboptimal resistance ( $R_s, R_{sh}$ ) of the device as shown by diode model schematic below in (f).

parameters. SCAPS is an open-source code and can be obtained from Prof Marc Burgelman, University of Gent. [27]

### 3. Results and discussion

The cross-sectional FESEM image of Caesium lead triiodide ( $\text{CsPbI}_3$ ) perovskite-based solar cell revealing device configuration is depicted in Fig. 2. Fig. 2(b) shows the surface morphology of  $\text{CsPbI}_3$  film. It shows the crystallinity, uniformity, size, and pinhole-free morphology of the spin-coated  $\text{CsPbI}_3$  layer. The grain size of the deposited film is observed by the ImageJ software. The pinhole defect-free and crystalline, large grain manifests the functionality of the spin-coated  $\text{CsPbI}_3$  films. Fig. 2(a) shows the cross-sectional images of the  $\text{CsPbI}_3$  solar cell device, revealing the inside layer structure. The devices have an FTO substrate,  $\text{TiO}_2$  (ETL) thickness of 25 nm, photoactive  $\text{CsPbI}_3$  absorber thickness of 400 nm, and spiro (HTL) around 100 nm. It also reveals that the crystalline grain of  $\text{CsPbI}_3$  connects ETL directly to the HTL vertically with an uninterrupted photogenerated carrier pathway in an absorber. The diffraction peaks in XRD patterns in Fig. 2(c) contain the diffraction plane corresponding to  $\text{CsPbI}_3$  and FTO. Furthermore, the XRD peak intensity of the  $\text{CsPbI}_3$  layers corresponds to the  $\alpha$  phase.

Fig. 3 shows the J-V characteristic of some of the fabricated  $\text{CsPbI}_3$  devices measured under AM1.5G condition and (b) the corresponding efficiency distribution. The efficiency of the fabricated device is in the range of 7.85–8.82%. The performance parameter of the best cell is open-circuit photovoltaic  $V_{OC}$  of 1.03 V, a short-circuit photocurrent density  $J_{SC}$  of 19.2  $\text{mA cm}^{-2}$ , fill factor (FF) of 0.446, and corresponding to

a PCE of 8.8%. The reverse scan of J-V characteristics shows a similar skink feature. The forward and reverse scan at two different scan rates, 50 and 25 mV/s, is shown in the inset of Fig. 3(a). The low scan rate shows higher decay in FF. This might be due to the slow transient process within the  $\text{CsPbI}_3$  device. The J-V curve is abnormal, with a noticeable skink behaviour. The skink is an s-type curvilinear shape of the J-V plot, which depletes FF. This skink is observed repetitively in all device J-V plots. A similar skink signature in the J-V curve is also observed in other systems such as chalcogenides CIGS, CdTe, [20,28] perovskite [14]. In the following section, we explored the probable defect and assigned the defect mechanism responsible for such a skink feature in J-V of our FTO/TiO<sub>2</sub>/ $\text{CsPbI}_3$ /Spiro/Au device.

Before moving to the cause of skink, let us briefly summarize other structure-dependent defect signatures in J-V, schematically shown in Fig. 4. Crossover is the breakdown of the superposition principle; the dark and illuminated  $J_{SC}$  are equal, as shown in Fig. 4(a). (black line for dark and red line for illuminated J-V). Crossover is a well-known observation occurring due to the Schottky barrier at one of the contacts in the device. [29] The contact barrier forms a secondary junction (metal/HTL) where voltage drop occurs, in addition to the primary junction of perovskite/ETL, lowering the overall  $V_{OC}$  of the device. The presence of such a secondary junction as a contact barrier at the front or back contact causes crossover, as reported in the literature. [29–31] The diode model is shown in Fig. 4(b). Next, rollover, i.e., the condition of current saturation beyond the  $V_{OC}$  point and the plot becomes parallel to the voltage axis, as seen in Fig. 4(c). Rollover is assigned to the combined

**Table 1**

Summarises the various abnormal features observed in J-V characteristics of solar cell devices and their generating causes.

| Anomaly in J-V            | Cause  | System             | Ref.      |
|---------------------------|--|--------------------|-----------|
| Roll over                 | Work function along with bulk defects                                  | CZTS               | 15        |
|                           | Energy barrier at the front contact                                    | CdTe               | 28        |
| Crossover                 | Work function mismatch of metal contact generally with p-type absorber | CZTS               | 15        |
|                           | Back-contact barrier and a low absorber carrier density                | CdTe               | 30        |
| Straight Hysteresis Skink | Contact-to-contact built-in potential                                  | Si                 | 32        |
|                           | Poor shunt and series resistance                                       | –                  | 16        |
|                           | Ion migration and accumulation   | Perovskite         | 5         |
|                           | High conduction band offset  | CdTe               | 35        |
|                           | High valence band offset in conjunction with bulk defects              | CsPbI <sub>3</sub> | This work |

**Table 2**

The experimental device parameters used for the theoretical device. Our simulation is repeatable by using the below device description. [5,11,21,36]

| Contact Properties  | FTO  | Spiro                                |   |                      |
|---|--|--------------------------------------|---|----------------------|
| SRV electron (cm/s)   | $10^7$   | $10^5$                               |   |                      |
| SRV hole (cm/s)   | $10^5$   | $10^7$                               |   |                      |
| Work function ( $\varphi_m$ )   | flat band  | 4.5 eV                               |   |                      |
| Band offset (eV)  | $E_{CBO} = 0$  | $E_{VBO}$ = varied in range 0–0.5 eV |   |                      |
| Parameters  | Spiro  | CsPbI <sub>3</sub>                   | TiO <sub>2</sub>                          | FTO                  |
| Thickness (nm)  | 150  | 400                                  | 25  | 150                  |
| Band gap (eV)   | 3.4  | 1.7                                  | 3.2                                       | 3.4                  |
| Electron affinity (eV)  | 2  | 4.4                                  | 4.1                                       | 4.5                  |
| CB effective density of state $N_C$ ( $\text{cm}^{-3}$ ) $\times 10^{18}$ | 2.2  | 18                                   | 2.2                                       | 11                   |
| VB effective density of state $N_V$ ( $\text{cm}^{-3}$ ) $\times 10^{18}$ | 18   | 2.4                                  | 18  | 11                   |
| Electron/Hole thermal velocity (cm/s)                                     | $10^7$   | $10^7$                               | $10^7$                                    | $10^7$               |
| Electron mobility (cm <sup>2</sup> /Vs)                                   | –  | 0.3                                  | 50  | 30                   |
| Hole mobility (cm <sup>2</sup> /Vs)                                       | .005   | 0.4                                  | 50  | 5                    |
| Donor/Acceptor density, $N_D/N_A$ ( $\text{cm}^{-3}$ )                    | $10^{16}$  | $10^{14}$                            | $10^{18}$                                 | $10^{19}$            |
| Absorption coefficient (cm <sup>-1</sup> )                                | $10^3$   | $10^5$                               | $10^3$                                    | $10^3$               |
| Bulk defect   |  |                                      |   |                      |
| Absorber  | $N_t$ ( $\text{cm}^{-3}$ ) varied in the range $10^{13}$ – $10^{15}$ | Charge state; type (0/-)/donor       | $\sigma_e, \sigma_h$ $10^{-14}, 10^{-14}$ | Uniform Distribution |
| HTL   | $N_t$ ( $\text{cm}^{-3}$ ) $10^{13}$ – $10^{14}$                     | Charge state; type (0/-)/donor       | $\sigma_e, \sigma_h$ $10^{-14}, 10^{-14}$ | Uniform Distribution |
| Interface Defects   |  |                                      |   |                      |
| Interface (Perovskite/HTL)  | Interface defect density ( $\text{cm}^{-2}$ ) $10^{12}$              | Charge state; type Neutral           | $\sigma_e, \sigma_h$ $10^{-14}, 10^{-14}$ | Uniform Distribution |

presence of the Schottky contact barrier and the bulk defects in the device. This rollover behaviour is persistently observed in the thin film solar cell family of CdTe. [32,35] Fig. 4(d) shows the diode model with a

secondary junction and small shunt resistance  $R_{Sh}$  (depicting the internal recombination path). Another feature is the linear J-V plot, as shown schematically in Fig. 4(e). This linear feature is observed for the device's suboptimum resistance values ( $R_S$  = high,  $R_{Sh}$  = low). The  $V_{OC}$  and  $J_{SC}$  are negligibly affected, but the fill-factor (FF) is significantly reduced for moderately suboptimal resistance values. [15] Table 1 presents abnormal J-V feature's one-to-one relation to their generating causes.

To explore the device design parameters responsible for generating skink in the device, we theoretically replicated our device with parameters, as shown in Table 2. The physical model of the CsPbI<sub>3</sub> solar cell device is schematically shown in Fig. 5. The device parameters, such as bandgap, energy level, and stack layers, are shown in the schematic. We have introduced the VBO and bulk defects in the device to replicate the experimentally observed skink in J-V.

We simulate CsPbI<sub>3</sub> perovskite device using SCAPS 1-D, which solves the Poisson and drift-diffusion equations at the junction under various illumination and biasing conditions to simulate J(V), C(V) and C(f), quantum efficiency curve, band diagram, recombination current, etc. across p-i-n heterojunction optoelectrical solar cell device. Applying relevant boundary conditions at the interfaces and different contacts, SCAPS solves the coupled differential equations in ( $\Psi$ , n, p) or ( $\Psi$ ,  $E_{Fn}$ ,  $E_{Fp}$ ).

$$J_n = -\frac{\mu_n n}{q} \frac{dE_{Fn}}{dx} \quad (1)$$

$$J_p = \frac{\mu_p p}{q} \frac{dE_{Fp}}{dx} \quad (2)$$

$$-\frac{dJ_n}{dx} - U_n + G = \frac{dn}{dt} \quad (3)$$

$$-\frac{dJ_p}{dx} - U_p + G = \frac{dp}{dt} \quad (4)$$

$$\frac{d}{dx} \left( \epsilon_0 \epsilon_r \frac{d\Psi}{dx} \right) = -q \left( p - n + N_D^+ - N_A^- + \frac{\rho_{def}}{q} \right) \quad (5)$$

Where  $\Psi$  is the electrostatic potential,  $\epsilon_0$ ,  $\epsilon_r$  is the permittivity of vacuum and semiconductor, n and p is the respective carrier density and  $N_D^+$ ,  $N_A^-$  is the density of donors and acceptors,  $\rho_{def}$  is the charge density of defects,  $J_n$ ,  $J_p$  is the individual electron and hole current density,  $E_{Fn}$ ,  $E_{Fp}$  is the electron, and hole Fermi level  $\mu_{p/e}$  is the hole/electron mobility, G is the generation rate, U is the recombination rate. Equations (1) and (2) are the charge carrier transport, 3–4 are the electron and hole-continuity equations, and equation (5) is the Poisson equation. SCAPS can replicate experimentally observed phenomena in solar cell devices such as light soaking, impurity photovoltaic effect, multijunction, tunnelling effect, J-V hysteresis, bandgap grading, etc., using appropriate conditions, defect models, script files, and recorder setup. One can replicate our results using these parameter details. The obtained results from the SCAPS are processed in MATLAB and plotted using the Origin. The

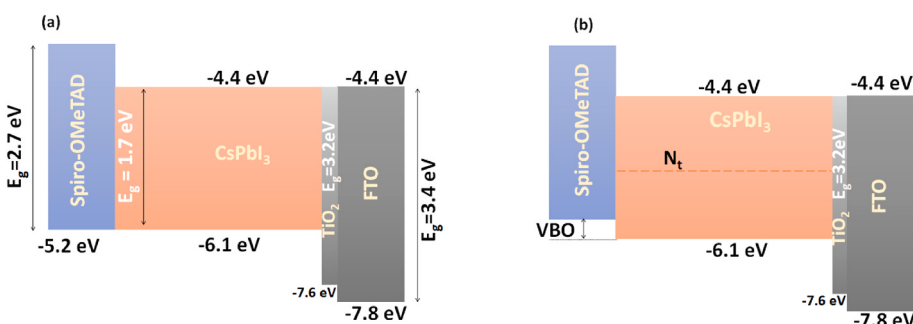
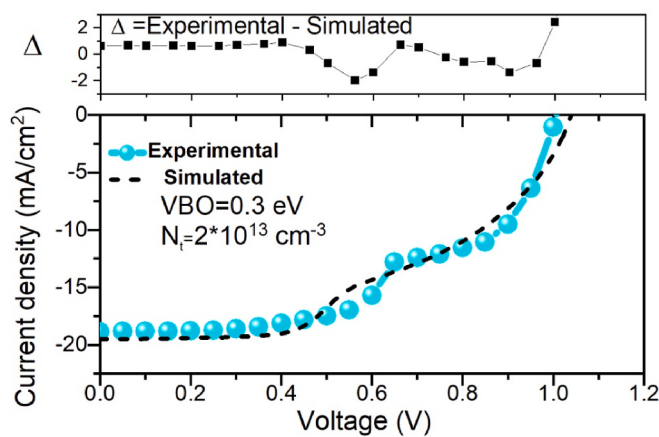


Fig. 5(a). The schematics of the CsPbI<sub>3</sub> device with corresponding bandgap, the different layers' conduction and valence energy levels. (b) The device's schematic with VBO and bulk defect density ( $N_t$ ) varied to fit the simulated JV with the experimental JV characteristics.



**Fig. 6.** The benchmarking of the physical model of device is established by overlapping the experimental and simulated J-V plots. The difference  $\Delta$  is also plotted to show the extent of overlapping.

benchmarking of the physical model of the device is performed. The comparative experimental and simulated J-V is plotted to show the extent of overlapping in Fig. 6. The difference between the experimental and simulated curve (marked by  $\Delta$ ) is also plotted to show the veracity of simulation in replicating the skink feature.

We run two simulations of our device FTO/TiO<sub>2</sub>/CsPbI<sub>3</sub>/Spiro/Au. In one, we have kept the ideal value, and in the second, we have introduced the valence band offset (VBO) of 0.4eV at the HTL/perovskite interface and bulk defect ( $N_t$ ) in the CsPbI<sub>3</sub> absorber layer. Fig. 7(a) shows a general device configuration of HTL/perovskite/ETL and corresponding near-perfect, abnormality-free J-V curve Fig. 7(b). We have introduced VBO at the HTL/Perovskite interface and interface defects in perovskite, and the schematic is shown in Fig. 7(c). This theoretical device replicates the skink behaviour in Fig. 7(d), which was observed experimentally. Skink is the reduction of current at a positive biasing voltage ( $>0$ ) within the power-producing quadrant and recovery of current at a higher positive forward bias (generally in the 1<sup>st</sup> quadrant). The curvilinear feature (s shape) we observed in our CsPbI<sub>3</sub> device is probably caused by the high VBO barrier at the HTL/perovskite interface in the device configuration in the presence of a bulk defect in the CsPbI<sub>3</sub> absorber layer. To establish and validate this statement, we show

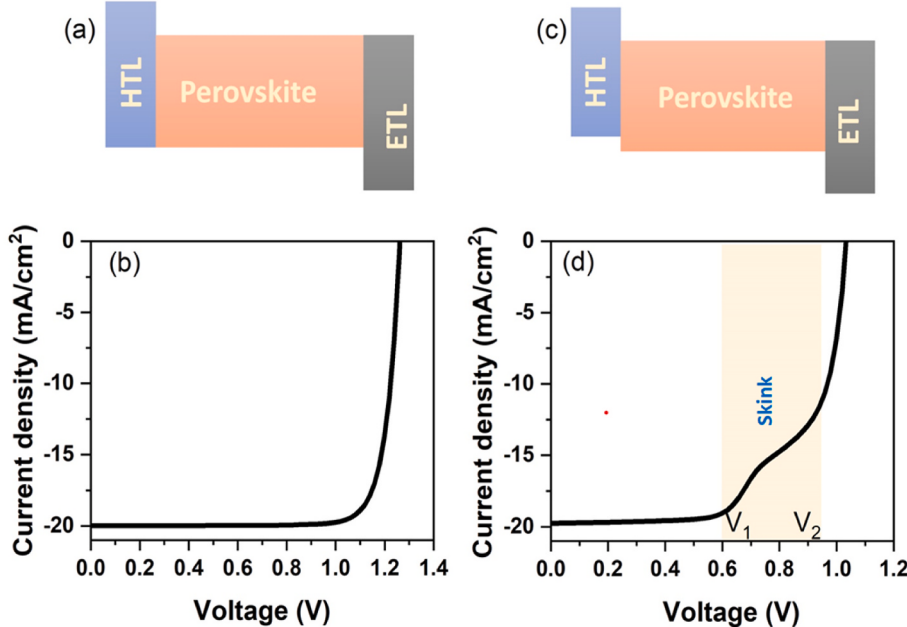


**Fig. 7.** (a) The schematic of the device and corresponding J-V plot as observed in simulation (b), (c) The device schematic with VBO (valence band level mismatch at HTL/perovskite interface) and corresponding J-V plot with a noticeable skink feature (d). The marked region in (d) shows a decrease in current.

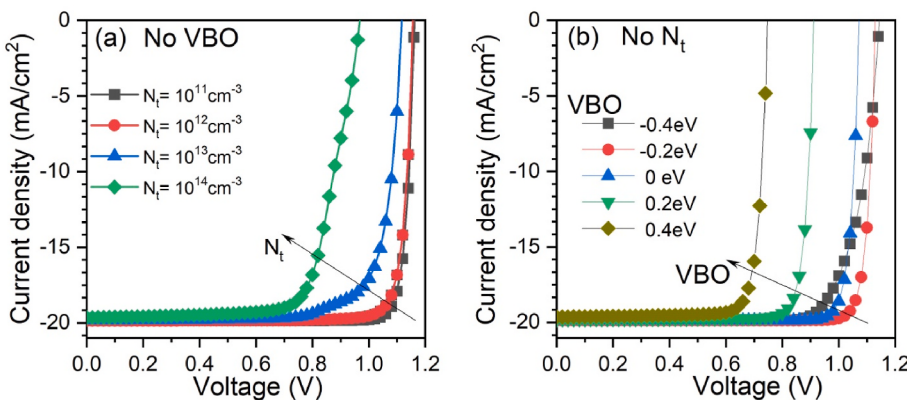


**Fig. 8.** The simulated J-V device characteristics for defect density variation and VBO = 0 (a), For VBO variation in the absence of CsPbI<sub>3</sub> bulk defects (b).

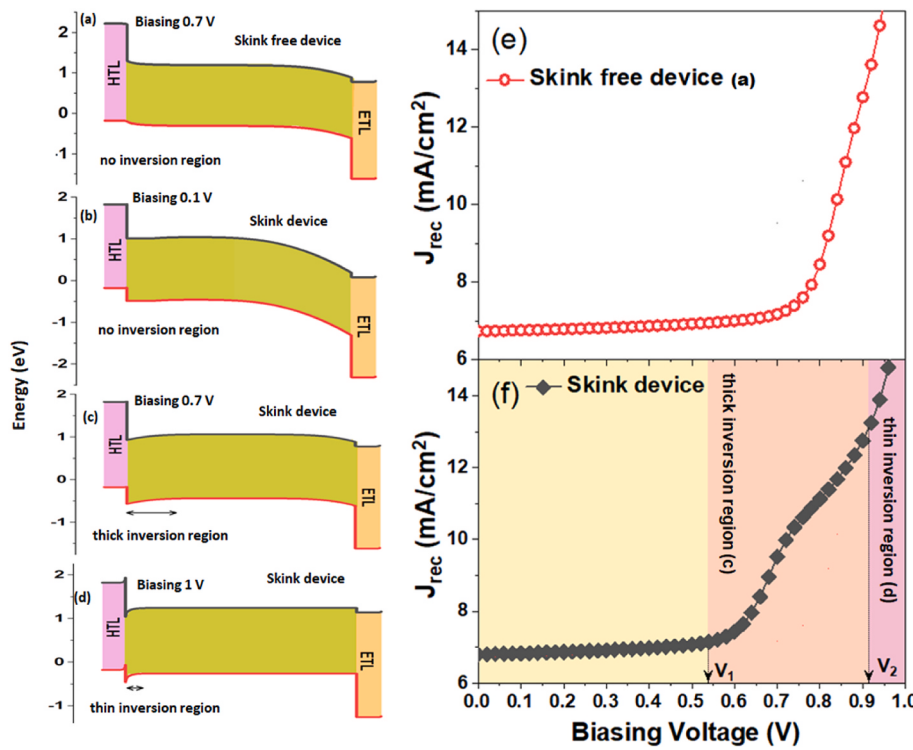


**Fig. 9.** (a) Shows the band diagram at the applied voltage of 0.7 V for skink free device. (b-d) shows the band diagram evolution with applied biasing voltage. The inversion region thickness variation at the HTL/perovskite junction with applied biasing voltage is highlighted in (b-d). The recombination current  $J_{rec}$  is compared for the skink-free device (e) and the skink device (f). The marked region shows the skink in thick inversion regions.

the variation of skink shape with the variation in VBO, defect density, and mobility. Thus, pin-pointing the recombination mechanism which could replicate such a skink in J-V of perovskite solar cells. The observed J-V plots in the two cases of Fig. 7(b,d) have identical  $J_{SC}$  values and decreased  $V_{OC}$  and FF due to the skink. We could replicate the experimentally observed phenomena by tuning VBO and simultaneously varying the acceptor defect density in the absorber layer. Various aspect of the skink phenomena is discussed in the next section. Non-ideal energy offsets by mean of VBO variation and the high bulk defect causes various degrees of skink phenomena numerically. [20]

Fig. 8 shows the individual impact of VBO and defects on the J-V characteristics of the device. Fig. 8(a) shows the device J-V for defect density ( $N_d$ ) variation in CsPbI<sub>3</sub> when the VBO at HTL/CsPbI<sub>3</sub> is taken to be 0. As shown, the  $V_{OC}$  and FF are sensitive to the defect density and decrease with increasing defect density. Fig. 8(b) shows the device J-V for VBO variation at HTL/CsPbI<sub>3</sub> interface. In this case, we have not taken bulk defects in the CsPbI<sub>3</sub>. The J-V shows a decrease in the  $V_{OC}$  and efficiency for the positively increasing VBO. Efficiency decreases for higher negative VBO. The J-V plot is maximum for the VBO = -0.2 eV. The valence band offset (VBO) occurs due to a mismatch of electron affinity (EA) in HTL and the perovskite layer of heterojunction. VBO is given by the difference of VBO = (Eg + EA)<sub>Perovskite</sub> - (Eg + EA)<sub>HTL</sub>, where Eg is the bandgap. It is the break at the valence band (Ev) levels of the perovskite absorber and HTL layer. VBO offers a Schottky barrier with resistance given by [33,34].

$$R = \frac{Ke^{\left(\frac{VBO_{Barrier}}{KT}\right)}}{qAT} \quad (6)$$

Where the symbols have usual meaning. Highly negative VBO acts as a barrier for hole transport, however small negative values are acceptable as the resistance will be low according to equation (6). [33,34]

As shown by the band diagram simulation in Fig. 9(a-d), the inversion region thickness depends on biasing voltage. This modulation of

accumulation region thickness at the HTL/Perovskite interface with high VBO and bulk defects trigger recombination at the HTL/Perovskite interface. At low biasing voltage, inversion region thickness is high; thus, the current decreases, and at high biasing voltage, thickness is reduced; therefore, the current resumes. This causes a notable reduction in FF by modifying the J-V curve into a curvilinear s shape. Fig. 9(e and f) shows the comparative recombination current  $J_{rec}$  of both cases of Fig. 9(a,c). The modulation of band bending at the secondary junction (HTL/Perovskite) with applied biasing causes a skink in the device.

The  $V_{OC}$  will be dropped at the primary junction (V<sub>Perovskite/ETL</sub>) and a secondary junction due to the Schottky barrier at (V<sub>Perovskite/HTL</sub>). The barrier at the back contact (under a high barrier offset) will control the current flow given by voltage drop across the secondary junction, V<sub>Perovskite/HTL</sub>, and the net current flow.

$$V = \begin{cases} \frac{nKT}{q} \ln \left( \frac{J_{SC}}{J_0} + 1 \right), & V < V_1 \\ \frac{nKT}{q} \ln \left( \frac{J_{SC}}{J_0} \right) \left( \frac{Ke^{\left(\frac{VBO_{Barrier}}{KT}\right)}}{RqAT} \right), & V_1 < V < V_2 \\ \frac{nKT}{q} \ln \left( \frac{J_{SC}}{J_0} \right), & V_2 < V \end{cases} \quad (7)$$

Where the symbols have the usual meaning,  $V_1$  and  $V_2$  are marked in Fig. 7(d).

This recombination mechanism is voltage-dependent in the presence of a VBO. For low voltage, depletion is minimal; thus no deviation in current; at high voltage, depletion region thickness is thin, therefore no impact on current flow. However, in mid applied voltage region ( $V_1$  to  $V_2$ ) current is reduced. The defects in the perovskite bulk bring about SRH recombination, lowering the number of hole carriers at the interface. Fig. 10(a) shows the evolution of the skink feature in J-V upon increasing defect density for a constant VBO of 0.4 eV. Fig. 10(b) shows the skink variation for VBO variation under a constant bulk defect of CsPbI<sub>3</sub>. VBO and defect density causes the different shape of the skink;

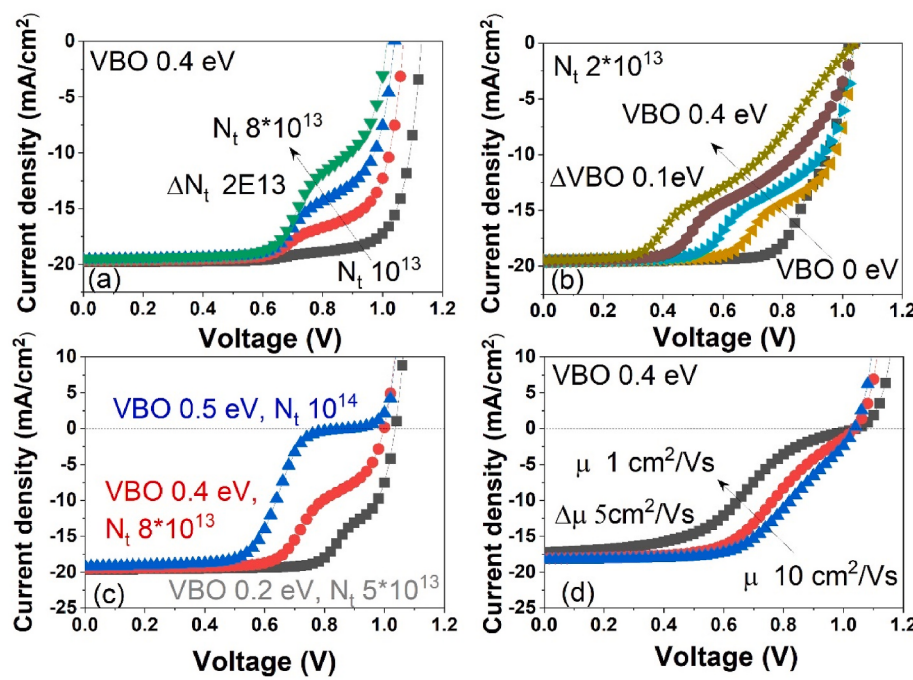


**Fig. 10.** (a) The impact of defect density variation in the presence of VBO on skink feature in J-V characteristics of the device. (b) The simulated effect of VBO variation on the J-V characteristic. (c) The modest to high skink feature for various VBO and defect density combinations. (d) The skink feature appears for hole mobility variation under high VBO in the  $\text{CsPbI}_3$  perovskite solar cell.

one lowers the voltage while the latter current. Fig. 10(c) shows the skink variation under the VBO and defect density variation. At high VBO (0.5 eV) and relatively high defect density ( $10^{14} \text{ cm}^{-3}$ ), a steep skink feature with high overlapping with the voltage axis is observed, as shown in Fig. 10(c). The high defect density lowers the majority carrier mobility in the absorber. We simulated the impact of the majority (hole) carrier mobility in the  $\text{CsPbI}_3$ . The lowering carrier mobility with a high valence band offset is observed to generate the skink feature in the J-V curve, as shown in Fig. 10(d).

To summarize, VBO and bulk defects are crucial for device performance. To control defect, trap regulation should be implemented in synthesis to decrease trap density within the  $\text{CsPbI}_3$  absorber layer. Techniques such as synthesis with additives such as dimethylammonium iodide,  $\text{InI}_3$ , which cause large grain growth [36–38] and intermediate-phase-modified crystallization, could be incorporated as trap regulation to decrease trap density within the  $\text{CsPbI}_3$  absorber layer. [39,40] The passivation of Spiro-OMeTAD film as the interface of HTL(Spiro-OMeTAD)/ $\text{CsPbI}_3$  to achieve  $\text{VBO} = 0$  is crucial. The energy level, especially the highest occupied molecular orbital HOMO level, can be varied by variation in the composition of Spiro-OMeTAD. [41] VBO and bulk defects have a severe impact on FF and device performance.

#### 4. Conclusion

Skink feature is observed in the current density-voltage (J-V) curve of an inorganic perovskite  $\text{CsPbI}_3$  solar cell device with experimental efficiency reaching 8.8%. The skink is a curvilinear feature with the reduction of current at a positive biasing voltage ( $>0$ ) within the power quadrant (4th quadrant) and recovery of current at a higher positive forward bias (near  $V_{\text{OC}}$ , generally in the 1<sup>st</sup> quadrant). Modelling of our device discerns that valence band offset (VBO) at the HTL/perovskite junction and high bulk defects can tune and achieve various degrees of skink feature. The moderately high offset barrier at the HTL/perovskite interface (with a value of 0.4 eV) fosters a skink in a  $\text{CsPbI}_3$  solar cell device, severely decreasing the fill factor and generating a curvilinear shape feature in J-V. The importance of band offset and sensitivity of device performance toward device design parameters is demonstrated in

this study which will be helpful in discerning efficiency limiting faults in experimental devices.

#### CRediT authorship contribution statement

**R Thandaiah Prabu:** Data curation. **Satyajeet Sahoo:** Writing – original draft. **K. Valarmathi:** Writing – original draft. **A Gnana Sagaya Raj:** Software. **Pranay Ranjan:** Writing – original draft, Software, Data curation. **Atul Kumar:** Writing – review & editing, Writing – original draft, Software, Investigation, Data curation, Conceptualization. **Amel Laref:** Writing – review & editing.

#### Declaration of competing interest

The authors declare that they have no known competing financial interests or personal relationships that could have appeared to influence the work reported in this paper.

#### Data availability

No data was used for the research described in the article.

#### References

- [1] A. Kojima, K. Teshima, Y. Shirai, T. Miyasaka, Organometal halide perovskites as visible-light sensitizers for photovoltaic cells, *J. Am. Chem. Soc.* 131 (17) (2009) 6050–6051.
- [2] M.A. Green, E.D. Dunlop, J. Hohl-Ebinger, M. Yoshita, N. Kopidakis, X. Hao, Solar cell efficiency tables (version 56), *Prog. Photovoltaics Res. Appl.* 28 (2020) 629–638.
- [3] K.R. Maithili, D.N. Sangeetha, Y.N. Sudhakar, M.G. Mahesh, Review on persistent challenges of perovskite solar cells' stability, *Sol. Energy* 218 (2021) 469–491.
- [4] B. Parida, A. Singh, A.K.K. Soopy, S. Sangaraju, M. Sundaray, S. Mishra, S. Liu, N. Adel, Recent developments in upscaleable printing techniques for perovskite solar cells, *Adv. Sci.* (2022), 2200308.
- [5] A. Kumar, Numerical modelling of ion-migration caused hysteresis in perovskite solar cells, *Opt. Quant. Electron.* 53 (2021) 1–9, <https://doi.org/10.1007/s11082-021-02806-1>.
- [6] Q. Tai, Kai-Chi Tang, Feng Yan, Recent progress of inorganic perovskite solar cells, *Energy Environ. Sci.* 12 (2019) 2375.

- [7] J. Tian, Q. Xue, Q. Yao, N. Li, C.J. Brabec, H. Yip, Inorganic Halide Perovskite Solar Cells: Progress and Challenges, 2020, <https://doi.org/10.1002/aenm.202000183>.
- [8] H. Yao, J. Zhao, Z. Li, Z. Ci, Z. Jin, Research and progress of black metastable phase CsPbI<sub>3</sub> solar cells Mater. Chem. Front. (2020), <https://doi.org/10.1039/d0qm00756k>.
- [9] Z. Shao, Z. Wang, Z. Li, Y. Fan, H. Meng, R. Liu, Y. Wang, A. Hagfeldt, G. Cui, S. Pang, A scalable methylamine gas healing strategy for high-efficiency inorganic perovskite solar cells, Angew Chem. Int. Ed. Engl. 16 (17) (2019) 5587–5591, <https://doi.org/10.1002/anie.201814024>, 58.
- [10] Hang Zhao, Xiaolong Liu, Xu Jia, Zhenzhen Li, Yao Fu, Honglu Zhu, Luxin Yan, Zhike Liu, Shengzhong Frank Liu, Jianxi Yao, Improvement of colloidal characteristics in a precursor solution by a PbI<sub>2</sub>-(DMSO)<sub>2</sub> complex for efficient non stoichiometrically prepared CsPbI<sub>2.8</sub>Br<sub>0.2</sub> perovskite solar cells, ACS Appl. Mater. Interfaces 12 (43) (2020) 48756–48764.
- [11] Liying Zhang, Boyuan Liu, Xiaoxiao Xu, Shendong Xu, Du Du, Hui Zhang, Tianle Guo, Haiying Zheng, Guozhen Liu, XuPan, Anchoring CsPbI<sub>3</sub> crystalline for stable and efficient perovskite solar cells with perfluorocarbon-assisted shield, Sol. Energy 228 (2021) 636–642.
- [12] Liying Zhang, Tianle Guo, Boyuan Liu, Du Du, Shendong Xu, Haiying Zheng, Liangzheng Zhu, Xu Pan, Guozhen Liu, Intermediate-phase-modified crystallization for stable and efficient CsPbI<sub>3</sub> perovskite solar cells, ACS Appl. Mater. Interfaces 14 (17) (2022) 19614–19622.
- [13] I. Jin, B. Parida, J.W. Jung, Simultaneously enhanced efficiency and ambient stability of inorganic perovskite solar cells by employing tetramethylammonium chloride additive in CsPbI<sub>2</sub>Br, J. Mater. Sci. Technol. 102 (2022) 224–231.
- [14] J. Liu, G. Wang, K. Luo, X. He, Q. Ye, C. Liao, J. Mei, Understanding the role of the electron-transport layer in highly efficient planar perovskite solar cells, ChemPhysChem (2017), <https://doi.org/10.1002/cphc.201601245>.
- [15] A. Kumar, A.D. Thakur, Comprehensive loss modeling in Cu<sub>2</sub>ZnSnS<sub>4</sub> solar cells, Curr. Appl. Phys. 19 (2019) 1111–1119.
- [16] A. Kumar, P. Ranjan, Defects signature in  $V_{OC}$  characterization of thin-film solar cells, Sol. Energy 220 (2021) 35–42.
- [17] Q. Chen, B.S. McKeon, S.Y. Zhang, F. Zhang, C. Hu, T.H. Geroer, M.W. Wanlass, D.J. Smith, Y. Zhang, Impact of individual structural defects in GaAs solar cells: a correlative and in operando investigation of signatures, structures, and effects, Adv. Opt. Mater. 9 (2021), 2001487.
- [18] B. Das, Z. Liu, I. Aguilera, U. Rau, T. Kirchartz, Defect Tolerant Device Geometries, 2020 arXiv:2008.13684.
- [19] K. Decock, S. Khelifi, S. Buecheler, F. Pianezzi, A.N. Tiwari, M. Burgelman, Defect distributions in thin film solar cells deduced from admittance measurements under different bias voltages, J. Appl. Phys. 110 (2011), 063722.
- [20] P.J. Roland, K.P. Bhandari, R.J. Ellingson, Reports Frequently Attribute the Behavior to the Presence of Non-ideal Energy Offsets at One or Both Contacts, 2016, <https://doi.org/10.1109/PVSC.2016.7750234>.
- [21] H. Xie, J. Xu, C. Gao, J. Zhang, C. Gao, X. Liu, Lead acetate precursors for preparing CsPbI<sub>3</sub> light harvester layers of inorganic perovskite solar cells, Sol. Energy 222 (2021) 212–218.
- [22] SCAPS Manual, Marc Burgelman, Koen Decock, Alex Niemegeers, Johan Verschraegen, Stefaan Degraeve, Version: 18 may 2020.
- [23] A. Kumar, A.D. Thakur, Role of contact work function, back surface field, and conduction band offset in Cu<sub>2</sub>ZnSnS<sub>4</sub> solar cell, Jpn. J. Appl. Phys. 57 (2018), 08RC05.
- [24] A. Kumar, A.D. Thakur, Design issues for optimum solar cell configuration, AIP Conf. Proc. 1953 (2018), 050022.
- [25] A. Kumar, P. Ranjan, Impact of light soaking on absorber and buffer layer in thin film solar cells, Appl. Phys. A 126 (2020) 397.
- [26] A. Kumar, Impurity photovoltaics and split spectrum for efficiency gain in Cu<sub>2</sub>ZnSnS<sub>4</sub> solar cells, Optik 238 (2021), 166783.
- [27] M. Burgelman, P. Nollet, S. Degraeve, Modelling polycrystalline semiconductor solar cells, Thin Solid Films 361–362 (2000) 527–532.
- [28] X. Li, K. Shen, Q. Li, Y. Deng, P. Zhu, D. Wang, Rollover behavior in current-voltage curve introduced by an energy barrier at the front contact in thin film CdTe solar cell, Sol. Energy 165 (2018) 27–34.
- [29] M. Köntges, R. Reineke-Koch, P. Nollet, J. Beier, R. Schäffler, J. Parisi, Light-induced changes in the electrical behavior of CdTe and Cu(In,Ga)Se<sub>2</sub> solar cells, Thin Solid Films 403–404 (2002) 280–286.
- [30] J. Pan, M. Gloeckler, J.R. Sites, Hole current impedance and electron current enhancement by back-contact barriers in CdTe thin film solar cells, J. Appl. Phys. 100 (2006) 12.
- [31] G. Agostinelli, E.D. Dunlop, D.L. Batzner, A.N. Tiwari, M. Kontges, Light dependent current transport mechanisms in chalcogenide solar cells, 3rd World, Conf. Photovolt. Energy Convers. 2003 (2014) 356–359.
- [32] J.E. Moore, S. Dongarkar, R.V.K. Chavali, M.A. Alam, M.S. Lundstrom, Correlation of built-in potential and IV crossover in thin-film solar cells, IEEE J. Photovoltaics 4 (2014) 1138–1148.
- [33] U. Rau, H.W. Schock, Electronic properties of Cu(In,Ga)Se<sub>2</sub> heterojunction solar cells-recent achievements, current understanding, and future challenges, Appl. Phys. Mater. Sci. Process 69 (1999) 131–147.
- [34] K. Wang, O. Gunawan, T. Todorov, B. Shin, S.J. Chey, N.A. Bojarczuk, D. Mitzi, S. Guha, Thermally evaporated Cu<sub>2</sub>ZnSnS<sub>4</sub> solar cells, Appl. Phys. Lett. 97 (2010), 143508.
- [35] Deng-Bing Li, Zhaoning Song, Rasha A. Awni, Sandip S. Bista, Niraj Shrestha, Corey R. Grice, Lei Chen, Geethika K. Liyanage, Mohammed A. Razooqi, Adam B. Phillips, Michael J. Heben, Randy J. Ellingson, Yanfa Yan, Eliminating S-Kink, To maximize the performance of MgZnO/CdTe solar cells, ACS Appl. Energy Mater. 2 (4) (2019) 2896–2903.
- [36] Xingtao Wang, Yong Wang, Yuetian Chen, Xiaomin Liu, Yixin Zhao efficient and stable CsPbI<sub>3</sub> inorganic perovskite photovoltaics enabled by crystal secondary growth, Adv. Mater. 33 (44) (2021), 2103688, <https://doi.org/10.1002/adma.202103688>.
- [37] Dr. Yong Wang, Xiaomin Liu, Dr. Taiyang Zhang, Xingtao Wang, Miao Kan, Jielin Shi, Prof. Yixin Zhao, The role of dimethylammonium iodide in CsPbI<sub>3</sub> perovskite fabrication: additive or dopant?, Angew. Chem. Int. Ed., Volume 58, Issue 46 p. 16691–16696 DOI: 10.1002/anie.201910800.
- [38] Xiaomei Li, Kaili Wang, Femi Lgbari, Chong Dong, Wenfan Yang, Ma Chang, Heng Ma, Zhao-Kui Wang, Liang-Sheng Liao, Indium doped CsPbI<sub>3</sub> films for inorganic perovskite solar cells with efficiency exceeding 17%, Nano Res. 13 (2020) 2203–2208, <https://doi.org/10.1007/s12274-020-2836-3>.
- [39] Liying Zhang, Tianle Guo, Boyuan Liu, Du Du, Shendong Xu, Haiying Zheng, Liangzheng Zhu, Xu Pan, Guozhen Liu, Intermediate-phase-modified crystallization for stable and efficient CsPbI<sub>3</sub> perovskite solar cells, ACS Appl. Mater. Interfaces 14 (17) (2022) 19614–19622, <https://doi.org/10.1021/acsami.2c04308>.
- [40] Sheng Fu, Nannan Sun, Jiabo Le, Wenxiao Zhang, Renjie Miao, Wenjun Zhang, Yongbo Kuang, Weijie Song, Junfeng Fang, Tailoring defects regulation in air-fabricated CsPbI<sub>3</sub> for efficient all-inorganic perovskite solar cells with  $voc$  of 1.225 V, ACS Appl. Mater. Interfaces 14 (27) (2022) 30937–30945, <https://doi.org/10.1021/acsami.2c07420>.
- [41] Laxmi Nakka, Yuanhang Cheng, Armin Gerhard Aberle, Fen Lin, Analytical review of spiro-OMeTAD hole transport materials: paths toward stable and efficient perovskite solar cells advanced energy and sustainability, Research 3 (2022), <https://doi.org/10.1002/aesr.202200045>.